Thermal Vacuum Cold Target for the Metop SG MicroWave Imager

Giuseppe Virone, *Senior Member, IEEE*, Giuseppe Addamo, *Member, IEEE*, Ada Vittoria Bosisio, *Member, IEEE*, Mario Zannoni, Luca Valenziano, Davide Rizzo, and Paolo Radaelli

***Abstract*—The assessment of the Metop-SG microwave imager radiometric performance is based on a complete set of thermal vacuum tests. Such an extensive experimental campaign requires the development of large calibration targets (black bodies) with controlled systematics and low residual uncertainties. The significant size of such targets, which are based on pyramidal emitting surfaces, does not allow for a complete minimization of the thermal gradients below the required accuracy level. This article presents the modeling approach that has been developed to deal with both such thermal gradients and the proximity of the baffle. Results on the frequency dependence of the cold target brightness temperature (ECCOSORB CR-117) are reported between 18.7 and 183 GHz. The complete uncertainty budget provides 1-sigma errors levels lower than 0.22 K. The systematic effect of thermal coupling with the earth target has been found as relevant as the coupling to the chamber. This interdependence requires a look-up-table approach to maintain the low uncertainty levels mentioned above.**

***Index Terms*—Microwave radiometry, calibration, pyramidal array, calibration target, thermal vacuum (TV), microwave imager (MWI).**

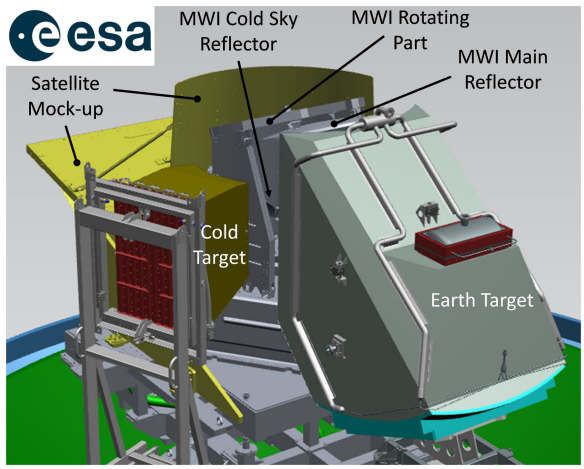

Fig. 1. Experimental configuration for the TV tests on the MWI instrument. Both calibraton targets and the satellite mock-up are visible (MLI is not reported for clarity).

I. Introduction

THE MICROWAVE imager (MWI) is a conical scanning radiometer operating from 18.7 to 183 GHz [1] that will be placed onboard the Metop second generation (SG) satellites. Its main scientific objectives are cloud and precipitation products [2], [3], snow and sea ice coverage and water vapor/temperature gross profiles.

The MWI radiometric performances, i.e., sensitivity, linearity and accuracy will be verified in thermal vacuum (TV) environment over the full operating temperature range of the instrument [4]. Such an activity requires the development of two TV calibration targets: the TV earth target (TV-ET, to be placed in front of the main reflector, see Fig. 1) to mimic a variable scene temperature from about 100 to 335 K and the TV cold target (TV-CT) operating at about 80 K (to be placed in front of the cold-sky reflector).

This article is focused on the brightness temperature estimation of the TV-CT, whose configuration is described in Section II. This task is particularly challenging owing to the overall temperature gradients that cannot be avoided on the emitting surface. All the emitting surfaces of the MWI targets (including the onboard hot target, not visible in Fig. 1) have the form of a periodic distribution of pyramids [5]–[8] to fit within the TV chamber size.

The modeling technique for the non-isothermal blackbodies is based on the cross-integral approach developed and validated in [9]–[11]. In this contribution, the cross-integral formula is derived from a circuit-based equivalent model (see Section III) which provides an intuitive visualization of the target emission as a cascade of attenuators.

The complete modeling strategy including the effect of the antenna pattern, the baffle and the target specular and diffuse reflection is described in Section IV.

Relevant results on the frequency dependence of the TV-CT brightness temperature are discussed in Section V-A, whereas a comprehensive evaluation of the uncertainty budget is discussed in Section V-B.

Manuscript received May 28, 2021; revised August 31, 2021; accepted September 22, 2021. Date of publication October 1, 2021; date of current version October 21, 2021. This work was supported in part by OHB as Instrument Prime of MWI and AirBus as prime contractor of Metop SG and in part by the European Space Agency. (*Corresponding author: Giuseppe Virone*.)

Giuseppe Virone, Giuseppe Addamo, and Ada Vittoria Bosisio are with the National Research Council of Italy, Istituto di Elettronica ed Ingegneria dell'Informazione e delle Telecomunicazioni, 10129 Torino, Italy (e-mail: giuseppe.virone@ieiit.cnr.it; giuseppe.addamo@ieiit.cnr.it; adavittoria.bosisio@ieiit.cnr.it).

Mario Zannoni is with the Dipartimento di Fisica "Giuseppe Occhialini," University of Milano Bicocca, 20126 Milan, Italy (e-mail: mario.zannoni@unimib.it).

Luca Valenziano is with the Istituto di Astrofisica Spaziale e Fisica Cosmica, Istituto Nazionale di AstroFisica, 40129 Bologna, Italy (e-mail: luca.valenziano@inaf.it).

Davide Rizzo and Paolo Radaelli are with the OHB Italia, 20151 Milan, Italy (e-mail: davide.rizzo@ohb-italia.it; paolo.radaelli@ohb-italia.it).

Digital Object Identifier 10.1109/JSTARS.2021.3117123

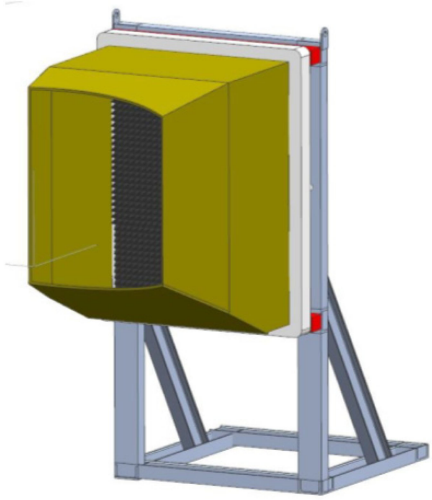

Fig. 2. Thermal vacuum cold target of MWI: baffle (dark yellow), pyramidal emitting surface (dark grey) and support structure (light grey). MLI is not reported for clarity.

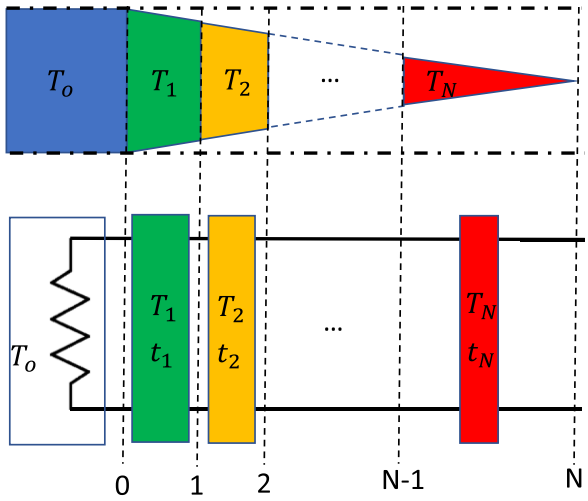

Fig. 3. Unit cell of a periodic black body and circuit model for the derivation of its brightness temperature.

Even if large metallic baffles have been conceived, the effects of thermal coupling to both the chamber and the TV-ET are significant. This problem has been quantified and solved with the look-up-tables reported in Section V-C. To the best of the authors knowledge, the brightness temperature evaluation with the effect of baffles, specular and diffuse target reflectivity, the corresponding uncertainty budget and the evaluation of the interdependence between multiple calibration targets are not yet available in the literature.

II. Thermal Vacuum Cold Target

The overall configuration of the TV-CT is shown in Fig. 2. The emitting surface (dark grey area) has the form of a periodic distribution of pyramids (characterized by high RF emissivity) above a thick high-thermal-conductivity metal baseplate. The overall size of the emitting surface is about 0.6 m $\times$ 0.8 m, it is composed of 20 tiles with 13 $\times$ 24 pyramids each. Cavity-based configurations [12]–[15] have been avoided because of their large longitudinal size. The heat exchanger based on LN2 pipes (visible in Fig. 1, dark red) is placed on the back of the emitting surface.

The target pyramids are made of an ECCOSORB-CR117 coating placed over a properly shaped aluminum pyramid to reduce the overall thermal gradient without impacting neither the RF nor the mechanical performance. The material has been characterized from 14 to 220 GHz by means of a proper set of waveguide samples (similarly to [16]) at both ambient and cryogenic temperatures. The obtained results are consistent with [17] where a free-space method has been instead adopted at ambient temperature.

The 4-mm-thick aluminum baffle is depicted with dark yellow. It provides a shielding effect from the thermal contributions of both the chamber and the ground support equipment that completes the test setup. The baffle is thermally controlled with LN2 pipes (same temperature of the emitting surface baseplate) and its inner surface is coated with Aeroglaze Z306 (high infrared emissivity, very low RF emissivity). This design solution further minimizes the thermal gradients on the emitting surface thanks to high thermal coupling to such a cold baffle. Both the outer baffle surface and the heat exchanger are instead covered with multilayer insulation (MLI, not shown for clarity).

III. Brightness Temperature of Nonisothermal Pyramid Black Bodies

This section presents the multiphysics calculation method that has been developed to compute the brightness temperature of nonisothermal black-bodies having a periodic structure and a slow-varying longitudinal profile of the unit cell. An example of unit cell is shown in Fig. 3 where the dash-dotted lines identify the periodic boundaries.

The black body unit cell has been divided in $N+1$ sections to exploit a circuit-based model for the calculation of the brightness/equivalent noise temperature. The slow-varying longitudinal profile of the unit cell and its absorbing material allows us to neglect the reflections between the various sections. The slow-varying profile also implies a very low higher-order mode excitation within the pyramid, which in turn justifies the exploitation of a single-mode equivalent circuit.

The equivalent circuit in Fig. 3 can be considered as cascade of attenuators. The first section with physical temperature T_0 is the closest one to the metal baseplate of the black body. Its radiation towards free space can be modelled as the product

$$T_o t_1 t_2 \cdots t_N \tag{1}$$

where t_n are the transmission coefficients of the various sections. The contribution of the second and last sections can be instead modelled as

$$T_1 \left(1 - t_1\right) t_2 \ \cdots t_N \tag{2}$$

and

$$T_N \left(1 - t_N\right), \tag{3}$$

respectively.

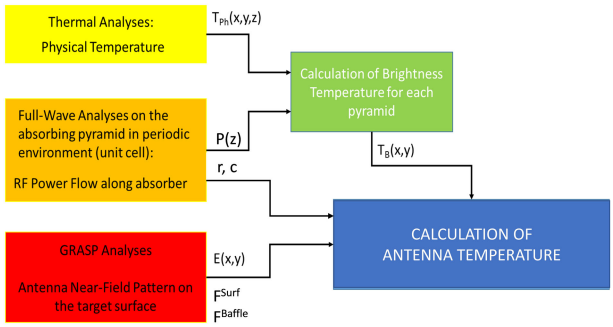

Fig. 4. Block diagram of the multiphysics calculation of the target brightness temperature from both thermal and RF analyses.

The physical temperatures T_n can be numerically evaluated using thermal analysis tools. The transmission coefficients t_n of the various sections can be instead evaluated by reciprocity.

As well known, the periodic structures can be efficiently analysed using Floquet modes excitation [18], [19], which are basically a discrete set of plane waves, and periodic boundaries (phase shift walls). This approach allows for an accurate computation of both the electromagnetic fields in the whole cell volume and the reflection to fundamental and higher order modes [20], [21]. For a given excitation direction, the RF power at each section P_n of the unit cell can be evaluated by integrating the computed power flow over the transverse section of the unit cell. Hence, the transmission coefficients of each attenuator section can be computed as

$$t_n = \frac{P_{n-1}}{P_n}. \tag{4}$$

After summation of all contributions and simplification of common terms, the final expression of the black-body equivalent noise temperature towards a given direction can be expressed as

$$T_B = T_0 \frac{P_0}{P_N} + \frac{1}{P_N} \sum_{n=1}^{N} T_n \left(P_n - P_{n-1}\right). \tag{5}$$

It should be noted that, according to reciprocity, the radiation direction is determined by the incident plane-wave defined in the full-wave electromagnetic analysis.

Finally, it is worth noting that for large values of *N* the series in (5) tends to the integral

$$\frac{1}{P_{\text{abs}}} \int T(z) \frac{dP(z)}{dz} dz \tag{6}$$

which contains the power absorption $\frac{dP(z)}{dz}$ along the longitudinal axis. P_{abs} is the total absorbed power. The effect of target reflection is discussed in Section IV. The term in (6) is identical to (7) in [10]. This confirms that the present circuit-based approach is equivalent to the methods reported in [10] and [11], which are based on the concept of local directional emissivity. The equivalent circuit in Fig. 3 facilitates an intuitive interpretation of the computed results presented in Section V.

IV. Modeling of Target Brightness Temperature

The block diagram of the complete modeling approach is shown in Fig. 4. The thermal analysis provides the three-dimensional distribution of physical temperature $T_{\text{Ph}}(x,y,z)$ along the target emitting surface. The full-wave analysis on the target unit cell (i.e. pyramid with periodic boundary conditions [20]) provides the RF power profile $P(z)$ along the pyramid as well as the specular reflectivity $r = |S_{11}|^2$ and coupling to higher order modes (diffuse reflectivity) $c = \sum_{n>1} |S_{n1}|^2$, where S_{n1} are the scattering parameters of the periodic structure for the considered Floquet modes [20]. Thermal and full-wave analyses are combined using the method described in Section III. This method produces the brightness temperature distribution $T_B(x,y)$ along the target surface.

The target brightness temperature is then defined as the equivalent noise temperature available at the output port of the radiometer antenna that is looking at the target. For this reason, this parameter is called T_A and is evaluated as

$$T_A = F^{\text{Surf}}\, T_A^{\text{Surf}} + F^{\text{Baffle}}\, T_A^{\text{Baffle}} \tag{7}$$

where F^{Surf} and F^{Baffle} are the fractions of integrated antenna radiation pattern $|E(x,y)|^2$ hitting the target surface and the baffle, respectively (computed from GRASP analyses, $F^{\text{Surf}} + F^{\text{Baffle}} = 1$) and

$$T_A^{\text{Surf}} = (1 - r - c) \frac{\iint T_B(x,y)\, |E(x,y)|^2 dxdy}{\iint |E(x,y)|^2 dxdy} + r\, T_{\text{Rec}}^{\text{BW}} + c\, \widehat{T_B} \tag{8}$$

is the brightness temperature of the target surface weighted with the antenna pattern (computed on the target emitting surface), where the effect of specular reflectivity r and coupling to higher order diffuse reflectivity c are also present. The overall approach is justified because both the physical temperature and the antenna pattern variation across the target surface are so smooth that the periodic (unit cell) approach is still valid. The losses of the radiometer antenna and the residual spillover (fraction of antenna pattern outside the baffle, which is below 10^{-5}) are not included in (7) because they will be accounted for at instrument level.

The specular reflectivity is associated to the backward noise radiated by the MWI radiometers $T_{\text{Rec}}^{\text{BW}}$, whereas the coupling c is associated to the average brightness temperature on the target surface $\widehat{T_B}$. This approximation relies on the fact that the higher order modes (diffracted plane waves oriented a few degrees away from the specular reflection) will not be directly coupled into the radiometer antenna. They will face multiple reflection inside the cavity formed by the instrument, the baffle, and the target surface. With good approximation, the target surface is the only cavity part with high emissivity in the frequency range between 18 and 183 GHz (the other parts are mainly made of metal or MLI). During the acquisition of the TV-CT, the large front apertures in the MWI rotating part (below the main reflector) will be oriented towards the semicylindrical sun shield of the satellite mock-up (visible in Fig. 1). In this configuration, the TV-ET is completely shut. Moreover, there is no direct (optical) view of the TV chamber thanks to the large size of the sunshield. A gap is present between the instrument and the sun shield, therefore,

a small fraction of energy emitted by the TV chamber could in principle enter the instrument by diffraction. A quantitative evaluation of such a coupling using EM analyses is very complex and time-consuming owing to the large structure size. Therefore, both the impact of this intrusion and possible multiple reflections inside the cavity were estimated by adding a large perturbation (about 50 K, 1-sigma) on the brightness temperature associated to the term c (the latter is in the order of -40 dB). The resulting contribution is in the order of 5 mK, which is negligible with respect to the other uncertainty terms that will be discussed in Section V-B.

For the same reasons mentioned above, $\widehat{T_B}$ has been also associated to the antenna radiation pattern hitting the baffle. It should be pointed out that the finite conductivity of the baffle can in principle affect the corresponding brightness temperature contributions ($T_A^{\mathrm{Baffle}}=\eta_B\,\widehat{T_B}+(1-\eta_B)\,T_{\mathrm{Ph}}^{\mathrm{Baffle}}$, where η_B is the reflectivity of the baffle and $T_{\mathrm{Ph}}^{\mathrm{Baffle}}$ is its physical temperature). However, experimental results on Aeroglaze-coated aluminum samples provided reflection levels η_B higher than -0.1 dB even approaching grazing incidence, the values of F^{Baffle} are kept below 10^{-3} owing to the large size of the target, and the physical temperature of the baffle is maintained as close as possible to the target one. For these reasons, the effect of baffle conductivity has been estimated in the order of 0.1 mK and hence negligible.

V. TV-CT Results

A. Frequency Behavior of Brightness Temperature

The thermal analyses have been carried out using both Thermica and Thermisol. Each pyramid is linked to the heat exchanger through its own aluminum base. The heat exchanger is modeled with an equivalent pattern of thermal resistances between the LN2 and the mounting interface plane of the tiles. The MWI instrument is represented by a reduced thermal model: an articulator representing nominal 45 r/min speed has been implemented. The complete lumped-parameter thermal model consists of about 100k nodes (in particular: 454 for baffle, 104 for MWI, 98420 for target, 1 for chamber shroud, 19 for TV-ET reduced thermal model).

The TV-CT will be used for complete TV cycles where the chamber and TV-ET temperatures will be varied from -150°C to 20°C and from 100 to 335 K, respectively. The worst-case is represented by the warmest chamber and TV-ET temperatures where their highest radiative contribution produces the largest tip-to-bottom gradient on the pyramids of the TV-CT (whose baseplate is instead maintained at 78 K). The results of the thermal analyses for such a worst-case operative condition, i.e., chamber at 20°C and TV-ET at 335 K are reported in Fig. 5. The average of $T_{\mathrm{Ph}}(x,y,z)$ along the z-axis (top) shows a transverse gradient of about 1 K. The longitudinal gradients (bottom) are about 5 K in the target center and even larger approaching the bottom edge.

The seven nodes that have been used to correctly describe the longitudinal temperature profile on each pyramid can be seen in Fig. 6(a) within the pyramid geometry: dashed line represents the aluminum profile whereas the solid line refers to ECCOSORB CR-117 coating. The pyramid base width is 8.6 mm, the total height is 45.8 mm, the absorber thickness is 1.4 mm. It should be noted that two thermal nodes are located on the tip where

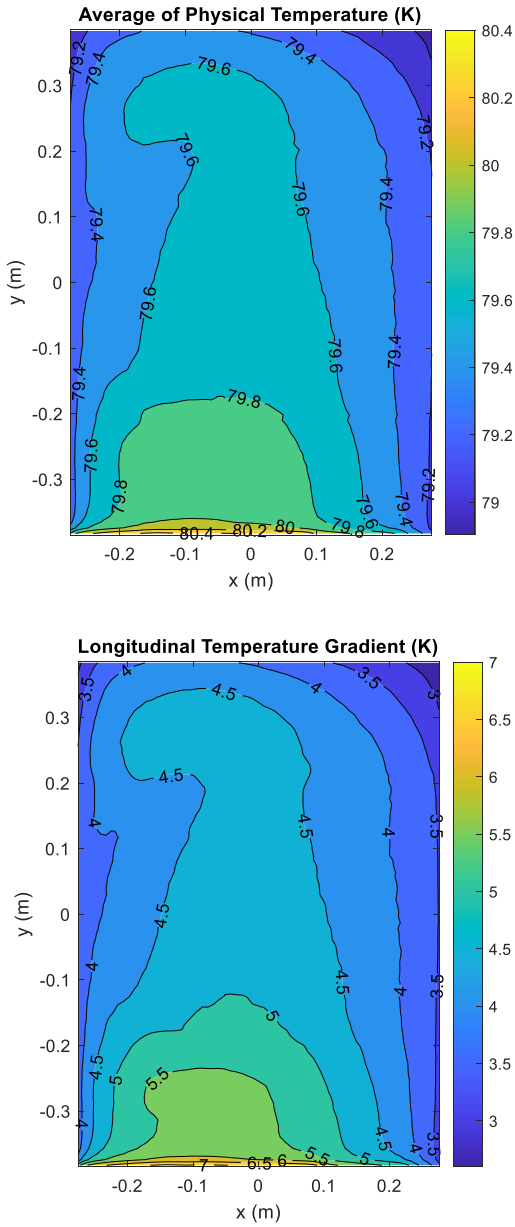

Fig. 5. Result of thermal analyses on the TV-CT emitting surface: average over pryamid axes (top), tip-to-bottom gradient along pyramid axis (bottom).

the metal is not present. The longitudinal temperature profiles for all the TV-CT pyramids are shown in Fig. 6(b). It can be confirmed that the maximum tip-to-bottom gradient is about 7 K. As already mentioned above, Fig. 5 (bottom) shows that pyramids with a 7-K gradient are only located in the proximity of the bottom edge of the target. From Fig. 6(b), it can be also observed that the physical temperature of the nodes is very close to 78 K for z $<$ 30 mm (the LN2 conditioned metal baseplate is at $z = 0$ mm). The node temperatures start to rapidly increase in the region where the metal pyramid (dashed line) is not present, i.e., $z > 35$ mm. This fact is due to the low thermal conductivity of the Eccosorb coating which is the only constituent material in the pyramid tip from z = 35 mm to z = 45.8 mm.

In Fig. 6, the thermal analysis data are compared to the results of the full-wave RF analyses performed on the pyramid unit cells

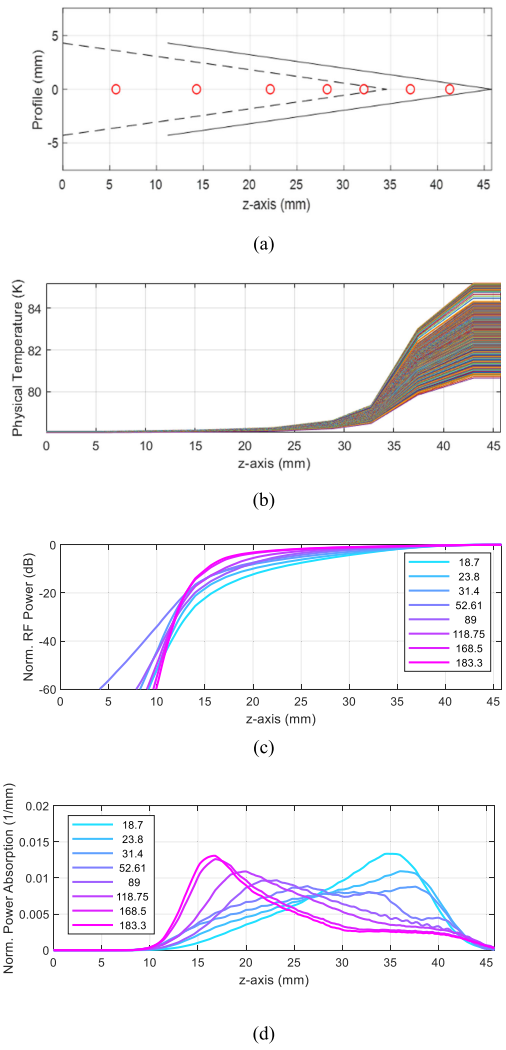

Fig. 6. Pyramid geometry (solid line: absorber, dashed line: metal) with nodes (red circles) used in thermal analysis (a). Result of thermal analyses on the TV-CT (b). RF power in the absorbers computed with plane wave incidence for all MWI channel frequencies (GHz) (c). Normalized power absorption (d).

at the MWI channel center frequencies [see Fig. 6(c)]. The RF analyses have been computed with periodic boundary conditions and plane-wave normal incidence using CST Microwave Studio. The power $P(z)$ is normalized at the tip ($z = 45.8$ mm). It can be observed that the power is gradually absorbed towards the pyramid base. Moreover, the lower frequencies are absorbed more rapidly than the higher ones. This fact is related to the better absorbing performance of the material in that frequency range (magnetic losses almost disappear at 90 GHz). Nevertheless, a transmission level of about -30 dB is achieved toward the base of the absorber pyramid ($z = 11.2$ mm). With reference to the circuit model in Fig. 3, it can be envisaged that the infinitesimal attenuators provide a region of maximum attenuation whose position along the z-axis is frequency dependent. The same consideration is also apparent in Fig. 6(d) where the normalized power absorption $\frac{1}{P_{\rm abs}}\frac{dP(z)}{dz}$ is shown. This is the quantity that weighs the temperature profile along the pyramid in (6). It should be noted that most of the RF power is absorbed from z<40 mm to z>20 mm at lower frequencies whereas the absorption peak shifts toward the pyramid base at higher frequencies. This result is consistent to the predictions in [10]. In this article, the phenomenon is even more significant owing to the larger frequency range (10:1) and the different absorbing material. In this framework, it is intuitive that, although the tip region (z>35 mm) exhibits the larger thermal gradient, it will not contribute significantly to the target brightness temperature, especially at higher frequencies. On the contrary, the overall brightness temperature will be instead dominated by the physical temperature of the inner region which is actually very close to the reference one (baseplate at 78 K). Even if the tip region does not significantly contribute to the absorption at high frequencies (it is quite transparent for RF), such a region is important because it produces the required impedance matching from free space to the inner sections of the absorber.

This basic consideration is reflected in the results obtained with the cross-integral calculation (see Section III). Figs. 7 (top) and 8 (top) show the brightness temperature distribution $T_B(x,y)$ across the target surface, i.e. the brightness temperatures computed for each pyramid of the target by means of the cross-integral method. As expected, the brightness temperature at 183.3 GHz is lower than at 18.7 GHz because the larger contribution is produced by the (colder) central part of the pyramid (tip region is more transparent at higher frequencies, [see Fig. 6(d)].

The plots on the bottom of Figs. 7 and 8 show the contours plots of the antenna radiation pattern on the target surface computed with GRASP at 18.7 and 183.3 GHz, respectively. The results refer to the angular position where MWI will start the acquisition of the cold target (start cal). Similar results have been obtained for the stop cal angular position (5° from start cal). These data are used in the framework of the final calculation of the target brightness temperature in (8). It should be observed that the maximum of the antenna pattern does not correspond to the maximum of the brightness temperature distribution. This fact further reduces the impact of pyramid thermal gradients on the overall target brightness temperature value.

The curvature of the phase front and the corresponding angle of incidence on the pyramids has been also computed from GRASP analyses (not shown for brevity). Within the -35 dB antenna footprint, the angle of incidence is very close to 0° with respect to the z-axis. This justifies the normal incidence considered in the full-wave electromagnetic analyses.

Fig. 9 shows the target brightness temperature (equivalent noise temperature available at the output port of the radiometer antenna that is looking at the target) for all MWI channels computed from (7). As mentioned above, the brightness temperature is higher at the lower frequencies because the tip contribution is larger. Besides, at higher frequencies, the maximum of the narrower radiation patterns does not coincide with the maximum of the surface brightness temperature.

It should be noted that the difference between the computed brightness temperatures and the baseplate physical temperature (78 K) is smaller (1.6 K at 18 GHz, 0.65 K at 183 GHz) than the tip-base thermal gradient (which is about 5 K in the target center). This fact highlights the importance of the reported modeling activity. It should be mentioned that the relevant contribution in (8) is the first one. This happens because both specular and diffuse reflection is below -40 dB in the whole frequency range.

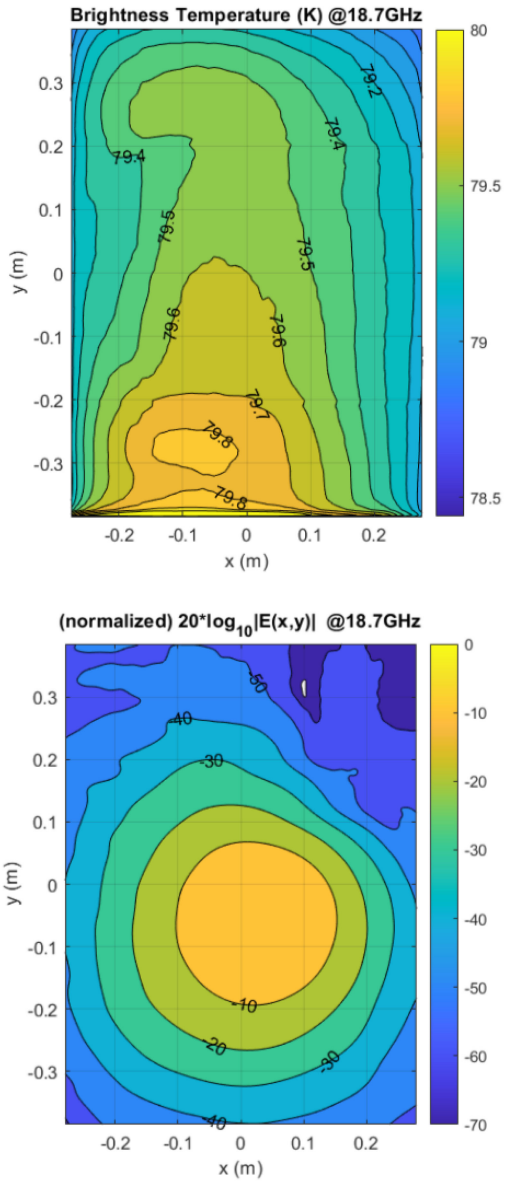

Fig. 7. Brightness temperature distribution at 18.7 GHz (top), antenna pattern distribution on the target at 18.7 GHz (bottom).

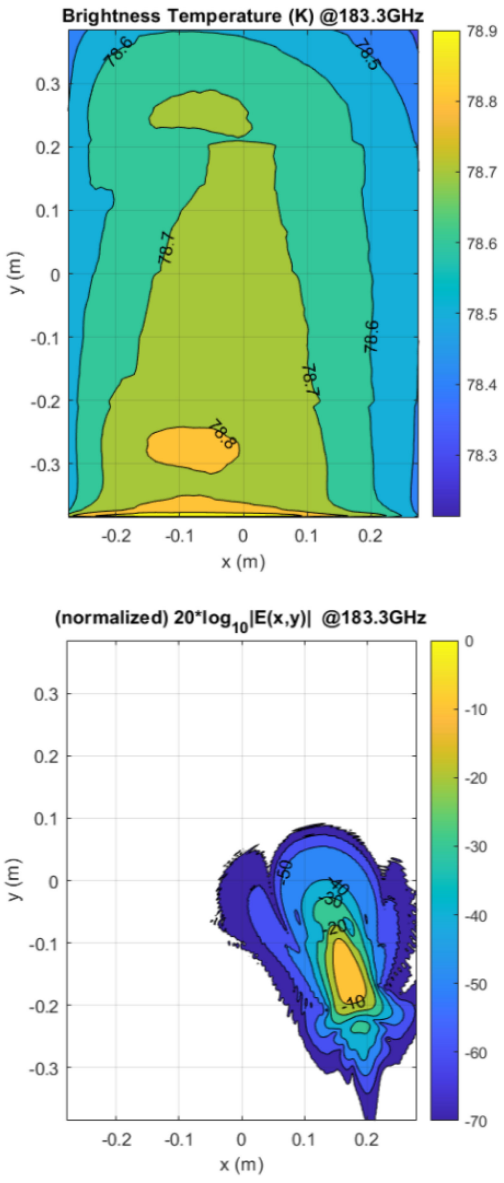

Fig. 8. Brightness Temperature distribution at 183.3 GHz (top), antenna pattern distribution on the target at 183.3 GHz (bottom).

B. Uncertainty Budget

The uncertainty on the brightness temperature values reported in Fig. 9 has been assessed by means of a perturbation approach. As reported above, the brightness temperature values at each frequency are derived from both thermal and RF models of the target. All the relevant model parameters have been varied within a range that is derived from the ECSS standards. The parameter description and the corresponding variations are given in Table I.

The variations of TV-CT brightness temperature with respect to the nonperturbed case in Fig. 9 are shown in Fig. 10 for the channels 18.7 and 183.3 GHz. It should be noted that both positive and negative error levels are reported. Their slight asymmetry with respect to 0 K is due the non-linearity of the thermal models. The baseplate thermometer uncertainty is also included in Fig. 10. All these values are considered as 1-sigma error contributions to the uncertainty budget. The obtained root

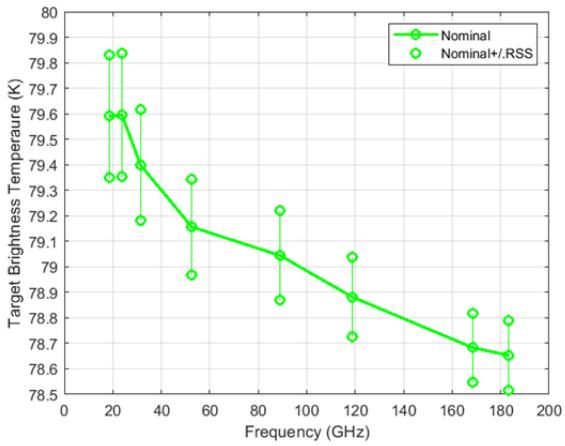

Fig. 9. TV-CT brightness temperature with 1-sigma error-bars for the worst—case operative condition, i.e., chamber at 20°C and TV-ET at 335 K.

TABLE I
VARIATION OF MODEL PARAMETERS FOR THE ESTIMATION OF THE CORRESPONDING ERROR BARS IN FIG. 10

Parameter	Variation (%)
MWI Dissipation	±20
Eccosorb Conductivity	±13
Aluminum Conductivity	±10
Contact Conductance between heat exchanger and tile baseplate	±17
MWI Emissivity	±5
Eccosorb Emissivity	±14
Eccosorb EM Parameters	±10
Radiometer Bacward Noise (T_{Rec}^{BW})	±30

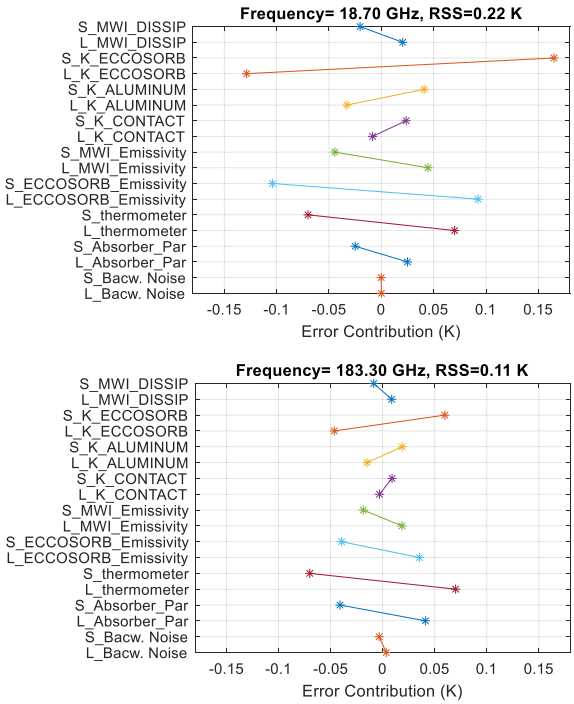

Fig. 10. TV-CT uncetainty budget at 18.7 and 183 GHz: 1-sigma error contributions for the worst—case operative condition, i.e., chamber at 20°C and TV-ET at 335 K.

sum square (RSS) values are 0.22 K at 18.7 GHz and decrease to 0.11 K at 183.31 GHz (see Fig. 10). The RSS bars are also shown in Fig. 9 for all frequency channels. It should be noted that such computed 1-sigma error bars are smaller than the predicted variation of brightness temperature versus frequency (about 1 K). This again highlights the importance of the modeling strategy.

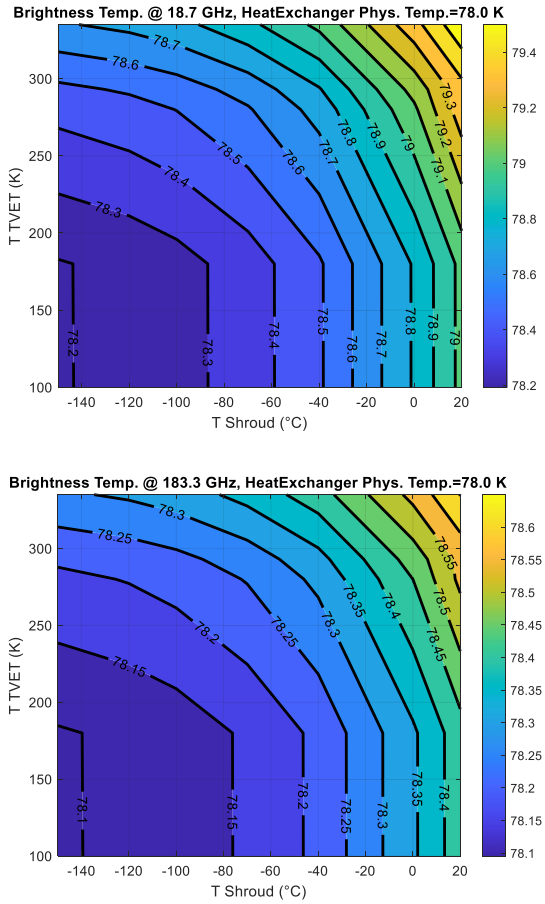

Fig. 11. Effect Shroud and TV-ET temperatures on TV-CT brightness temperature at 18.7 GHz (top) and 183.3 GHz (bottom).

The value of assumed uncertainty for the radiometer backward noise $T_{\mathrm{Rec}}^{\mathrm{BW}}$ is ±30 K (1-sigma, see Table I) because the real values were not known at the time of this analysis (nominal value was set to 120 K). However, thanks to the -40 dB specular reflection level of the target surface, this unknown does not have relevant impact on the uncertainty budget (see last item in Fig. 10).

As already mentioned above, the fraction of antenna pattern impinging on the baffle is below 10^{-3}, the average brightness temperature on the target surface $\widehat{T_B}$ is very close to the values of $T_B(x,y)$ within the antenna footprint, therefore, the contribution of F^{Baffle} variations of 2 dB (1-sigma) to the overall uncertainty budget are negligible (below 0.1 mK). Negligible error contributions were also obtained from variation of specular r and diffuse reflectivity c within 2 dB (1-sigma).

It should be mentioned that the present analysis does not include the effect of standing waves between the radiometer antenna and the TV-CT target [22]. Such a coherent effect can be kept into account at instrument level exploiting the full knowledge of each radiometer architecture (e.g., presence of isolator, other calibrators) and the corresponding noise parameters.

C. Coupling to the TV Chamber and the TV-ET

As mentioned above, the brightness temperature data in Fig. 9 are valid for the worst-case operative condition, i.e., maximum

temperature values for both chamber and TV-ET. This condition corresponds to the upper right corner of Fig. 11. As mentioned above, the TV-CT will be used for complete TV cycles where the chamber and TV-ET temperatures will be varied from -150°C to 20°C and from 100 to 335 K, respectively. All the operative conditions have been studied with the full approach presented in this article. The complete set of results is shown is Fig. 11. It is apparent that the effect of the TV-ET is as significant as the chamber one (shroud temperature). The sharp discontinuity of the contour plots around 180 K is due to a transition in the operation mode of the TV-ET. Above 180 K, the baffle of the TV-ET is no longer maintained at LN2 temperature, therefore, its contribution become significant on the gradients of the TV-CT. Such a coupling occurs because there is a view factor between the TV-ET and TV-CT baffle inner surfaces (Aeroglaze-coated) in the proximity of the corresponding apertures where the TV-CT baffle is not conditioned with LN2 (it is only conditioned in the proximity of its emitting surface to reduce the tip-to-bottom gradient on the pyramids). On the contrary, there is no direct radiative coupling between the two target emitting surfaces. The effect of reflections from MWI rotating part has been found to be less significant than the direct baffle coupling mentioned earlier.

For calibration purposes at instrument level, the data in Fig. 11 will be used as a look-up-table for the TV-CT brightness temperature. This approach has been selected instead of the reduced-order model proposed in [10] mainly because of the discontinuity in TV-ET contribution.

The variation of the TV-CT baseplate temperature within 77 and 79 K has been also computed obtaining the expected quasi-linear behavior.

VI. Conclusion

The design and performance estimation of the TV-CT for the MWI TV campaign has been presented. A multiphysics approach has been adopted to compute the brightness temperature in presence of longitudinal gradients, transverse gradients, frequency dispersion of RF absorber parameters and baffle reflection phenomena. The latter have been found to be negligible. This confirms the correct sizing of the TV-CT.

The offset of the TV-CT brightness temperature with respect to the physical temperature of the emitting surface baseplate is within 1.6 and 0.65 K at 18.7 and 183.3 GHz, respectively. This result has been achieved because of both the baffle cooling solution (which provides tip-to-bottom gradients of about 5 K in the target centre) and the overall multiphysics modelling approach.

The comprehensive uncertainty budget provided 1-sigma error values below 0.22 K, which are satisfactory for the MWI validation and prelaunch calibration.

The adjacent TV-ET target produces a very significant offset on the TV-CT brightness temperature. Besides the TV-CT baseplate temperature, both the effect of TV-ET and the chamber physical temperatures have been included in the TV-CT look-up-table that is required at instrument level.

Acknowledgment

The authors want to acknowledge Prof. N. Mandolesi (University of Ferrara, co-PI of the ESA mission Planck) for the fruitful discussions on this activity. We also want to acknowledge Christophe Malassingne (Airbus, Toulouse, France) and Nicola Gatti (Space Engineering, Rome, Italy) for the GRASP analyses. The view expressed herein can in no way be taken to reflect the official opinion of the European Space Agency.

References

[1] S. D'Addio *et al.*, "Microwave imager instrument for MetOp second generation," in *Proc. 13th Specialist Meeting Microw. Radiometry Remote Sens. Environ.*, 2014, pp. 236–239.

[2] D. W. Draper, D. A. Newell, F. J. Wentz, S. Krimchansky, and G. M. Skofronick-Jackson, "The global precipitation measurements (GPM) microwave imager (GMI): instrument overview and early on-orbit performance", *IEEE J. Sel. Topics Appl. Earth Observ. Remote Sens.*, vol. 8, no. 7, pp. 3452–3462, Jul. 2015, doi: 10.1109/JSTARS.2015.2403303

[3] N. Grody, J. Zhao, R. Ferraro, F. Weng, and R. Boers, "Determination of precipitable water and cloud liquid water over oceans from NOAA 15 advanced microwave sounding unit," *J. Geophys. Res.*, vol. 106, no. D3, pp. 2943–2956, Feb. 2001.

[4] T. Lupi *et al.*, "Microwave imager instrument for MetOp second generation: design and verification," in *Proc. 14th Specialist Meeting Microw. Radiometry Remote Sens. Environ.*, Apr. 2016, pp. 32–36.

[5] A. Schröder *et al.*, "Electromagnetic Design of Calibration Targets for MetOp-SG microwave instruments," *IEEE Trans. Terahertz Sci. Technol.*, vol. 7, no. 6, pp. 677–685, Nov. 2017, doi: 10.1109/TTHZ.2017.2757442.

[6] M. Bai, D. Xia and M. Jin, "Effects of coating material properties on the wideband reflectivity performance of microwave calibration targets," *IEEE Trans. Antennas Propag.*, vol. 65, no. 9, pp. 4909–4913, Sep. 2017, doi: 10.1109/TAP.2017.2731383.

[7] D. Gu, D. Houtz, J. Randa and D. K. Walker, "Reflectivity study of microwave blackbody target," *IEEE Trans. Geosci. Remote Sens.*, vol. 49, no. 9, pp. 3443–3451, Sep. 2011, doi: 10.1109/TGRS.2011.2125975.

[8] E. M. Twarog, W. E. Purdy, P. W. Gaiser, K. H. Cheung and B. E. Kelm, "WindSat on-orbit warm load calibration," *IEEE Trans. Geosci. Remote Sens.*, vol. 44, no. 3, pp. 516–529, Mar. 2006, doi: 10.1109/TGRS.2005.863300.

[9] A. Murk, A. Schröder, M. Winser, Yichen Qian and R. Wylde, "Temperature/absorption cross integrals and the validation of radiometric temperatures for space-based radiometers," in *Proc.10th Eur. Conf. Antennas Propag.*, 2016, pp. 1–3, doi: 10.1109/EuCAP.2016.7481870.

[10] A. Schröder, A. Murk, R. Wylde, D. Schobert, and M. Winser, "Brightness temperature computation of microwave calibration targets," *IEEE Trans. Geosci. Remote Sens.*, vol. 55, no. 12, pp. 7104–7112, Dec. 2017

[11] D. M. Jackson and A. J. Gasiewski, "Electromagnetic and thermal analyses of radiometer calibration targets," in *Proc. Int. Geosci. Remote Sens. Symp. Taking Pulse Planet, Role Remote Sens. Manag. Environ. Proc.*, 2000, pp. 2827–2829 vol. 7.

[12] A. Schröder and A. Murk, "Numerical design and analysis of conical blackbody targets with advanced shape," *IEEE Trans. Antennas Propag.*, vol. 64, no. 5, pp. 1850–1858, May 2016.

[13] S. Fernandez, A. Murk, and N. Kämpfer, "Design and characterization of a Peltier-cold calibration target for a 110-GHz radiometer," *IEEE Trans. Geosci. Remote Sens.*, vol. 53, no. 1, pp. 344–351, Jan. 2015.

[14] D. A. Houtz, W. Emery, D. Gu and D. K. Walker, "Brightness temperature calculation and uncertainty propagation for conical microwave blackbody targets," *IEEE Trans. Geosci. Remote Sens.*, vol. 56, no. 12, pp. 7246–7256, Dec. 2018, doi: 10.1109/TGRS.2018.2849647.

[15] A. Murk *et al.*, "Low mass calibration target for mm-wave remote sensing instruments," *IEEE Trans. Antennas Propag.*, vol. 61, no. 4, pp. 1547–1556, Apr. 2013.

[16] L. Valenziano *et al.*, "New RF data on ECCOSORB^{TM} CR/MF absorber," in *Proc. SPIE 9153, Millimeter, Submillimeter, Far-Infrared Detectors Instrum. Astron. VII*, Jul. 2014, Art. no. 91532X.

[17] I. Zivkovic, A. Murk, "Characterization of magnetically loaded microwave absorbers," *Prog. Electromagn. Res. B*, vol. 33, pp. 277–289, 2011

[18] A. Tibaldi, R. Orta, O. A. Peverini, G. Addamo, G. Virone and R. Tascone, "Skew incidence plane-wave scattering from 2-D dielectric periodic structures: analysis by the mortar-element method," *IEEE Trans. Microw. Theory Techn.*, vol. 63, no. 1, pp. 11–19, Jan. 2015, doi: 10.1109/TMTT.2014.2373360.

[19] S. Sandeep and A. J. Gasiewski, "Electromagnetic analysis of radiometer calibration targets using dispersive 3D FDTD," *IEEE Trans. Antennas Propag.*, vol. 60, no. 6, pp. 2821–2828, Jun. 2012, doi: 10.1109/TAP.2012.2194679.

[20] G. Addamo *et al.*, "Design and RF performance analysis of microwave radiometer calibration targets," in *Proc. IEEE 15th Specialist Meeting Microw. Radiometry Remote Sens. Environ.*, 2018, pp. 1–3, doi: 10.1109/MICRORAD.2018.8430708.

[21] S. Sandeep and A. Gasiewski, "Effect of geometry on the reflectivity spectrum of radiometer calibration targets," *IEEE Geosci. Remote Sens. Lett.*, vol. 11, no. 1, pp. 84–88, Jan. 2014, doi: 10.1109/LGRS.2013.2246914

[22] J. Randa, D. K. Walker, A. E. Cox and R. L. Billinger, "Errors resulting from the reflectivity of calibration targets," *IEEE Trans. Geosci. Remote Sens.*, vol. 43, no. 1, pp. 50–58, Jan. 2005, doi: 10.1109/TGRS.2004.839809.

Giuseppe Virone (Senior Member, IEEE) was born in Turin, Italy, in 1977. He received the Laure a degree in electronic engineering (summa cum laude) and the Ph.D. degree in electronics and communication engineering from the Politecnico di Torino, Turin, Italy, in 2001 and 2006, respectively.

He is currently a Senior Researcher with the Istituto di Elettronica e di Ingegneria Informatica e delle elecomunicazioni (IEIIT), Italian National Research Council (CNR). He was with the IEIIT, as a Research Assistant in 2002. He coordinated more than 15 scientific projects funded by both the industry and other scientific research organizations and joined more than 30 research projects as a collaborator. He authored 43 journal papers, 134 conference papers papers and three European patents. His research interests are in the design, numerical analysis and characterization of microwave and millimeter passive components for feed systems, antenna arrays, frequency selective surfaces, compensated dielectric radomes and industrial sensing applications.

Giuseppe Addamo (Member, IEEE) was born in Messina, Italy, in 1979. He received the Laurea degree (summa cum laude) in electronic engineering and the Ph.D. degree in electronic and communication engineering from the Politecnico di Torino, Turin, Italy, in 2003 and 2007, respectively.

In January 2007, he was with the Instituto di Elettronica e di Ingegneria dell'Informazione e delle Telecomunicazioni, Consiglio Nazionale delle Ricerche, Turin, Italy, as a Research Fellow, and in 2012, became a Researcher. He holds practical classes in courses on electromagnetic field theory and mathematical analysis with the Politecnico di Torino. His research interests are in the areas of microwave leaky antennas, dielectric radomes, high-power feed systems (e.g., orthomode transducers, microwave filters), corrugated horns, frequency-selective surfaces, and large dielectric radomes.

Ada Vittoria Bosisio (Member, IEEE) received the M.S. degree in electronic engineering and the Ph.D. degree in applied electromagnetism from the Politecnico di Milano, Milano, Italy, in 1991 and 1995, respectively.

During her Doctorate degree, she was involved in the Olympus and Italsat propagation experiments for the aspects related to propagation-oriented radiometry (Ka band). From 1995 to 1997, she was a Research Associate with the CETP/CNRS Laboratory, Vélizy, France, where she has been active in measurements and analysis of forest attenuation and scattering at 2 and 6 GHz. From 1997 to 1998, she was with CNET/France Telecom, Issy Les Mx, France, as an Ingenieur de Recherche, working on radio-wave effects induced by GSM on the environment and on individuals. From 1999 to 2001, she was with the Propagation Group, Politecnico, Milano, Italy, as a Research Associate working on satellite links at low elevation angle in *K*- and *W*-band and on propagation of TV broadcast and digital radio links over mountains through ray techniques. Since 2001, she has been a Researcher with Italian National Research Council, IEIIT Institute, Milano, Italy, working on remote sensing applications related to atmospheric science and tropospheric propagation. Her research interests include microwave radiometry and the interaction mechanisms between signal and complex media in the terrestrial biosphere.

Mario Zannoni was born in Milan, Italy, in 1969. He received the master's degree (summa cum laude) in physics and the Ph.D. degree in astronomy from the Università degli Studi di Milano, Milan, Italy, in 1994 and 2000, respectively.

He is currently an Associate Professor of astronomical instrumentation with the Università di Milano Bicocca, Milan, Italy, where he is responsible for the millimetric and cryogenic laboratory. He is a Member of National and International Astronomical Collaborations with a coordination role and he is responsible for the realization of scientific instrumentations and subsystems. He has authored or coauthored 64 journal articles and 60 conference papers. His research activity is focused in the cosmic microwave background polarization and related instrumentation.

Luca Valenziano received the master's degree in physics from Università degli Studi di Roma "La Sapienza", Rome, Italy, in 1992, and the Ph.D. degree in physics from Università degli Studi di Perugia, Perugia, Italy, in 1995.

He is a Senior Research Staff Member with INAF–Osservatorio di Astrofisica e Scienza dello Spazio, Bologna, Italy. From 1990 to 2005, he developed the cryogenic on-board calibrator for the Low Frequency Instrument on the ESA Planck satellite (Gruber Prize 2018 as member of the Planck core team). In 2007, he was among the proposers of a space mission, which later evolved in the Euclid project, adopted by the European Space Agency as the second Medium-size mission of the Cosmic Vision programme. He is the INAF scientific responsible for the Italian participation to Euclid; he leads the team that successfully delivered the national HW contribution to the Near-IR instrument, called NISP. He is actually leading the INAF team responsible for the Instrument Control Unit for the X-IFU instrument on the ESA L2 Athena mission. More recently, he took the role of Project Manager of the Camera system, the core of the payload module, for the ESA PLATO M3 mission. He was also the Project Manager for the High-resolution spectrograph HIRES for the ESO ELT during the Phase A. Since 2016, he has been responsible for the INAF presidential office for international and multilateral collaborations. He is author of more than 300 publications. His scientific activity is focused on experimental cosmology, mainly using space platforms. He devoted most of his research career to develop space technologies and implementing methods for their successful application to scientific projects.

Davide Rizzo was born in Verona, Italy, in 1985. He received the degree in space engineering from the Politecnico di Milano, Milan, Italy, in 2009.

He is currently a Senior Thermal Analysis, Design and Verification Engineer with OHB Italia S.p.A, Milan, Italy. He was with OHB Italia S.p.A. (formerly Carlo Gavazzi Space S.p.A.) in 2010. He worked on several ESA satellites, payloads and projects, such as AMS-02 (NASA, flown in 2011), Small GEO Hispasat 36W-1 (flown in 2017), Hexapod on SAGE III (flown in 2017), ASIM (flown in 2019). He is currently working on MWI Instrument (MetOp-SG payload) and CIMR. He has been responsible of several TVAC test campaigns and of Hispasat 36W-1 LEOP and commissioning. His activities concern the design, thermal analysis and test verification of spacecrafts and space payloads.

Paolo Radaelli was born in Italy, in 1967. He received the M.Sc. degree in physics from the Università degli Studi di Milano, Milan, Italy, in 1992.

He is currently a Senior System Engineer with OHB Italia S.p.A, Milan, Italy.